analytical chemistry

pubs.acs.org/ac Article

Multispectral Nanoparticle Tracking Analysis for the Real-Time and Label-Free Characterization of Amyloid-β Self-Assembly In Vitro

Colman Moore, Ryan Wing, Timothy Pham, and Jesse V. Jokerst*

Cite This: *Anal. Chem.* 2020, 92, 11590–11599 Read Online

ACCESS | Metrics & More | Article Recommendations | Supporting Information

ABSTRACT: The deposition of amyloid β (Aβ) plaques and fibrils in the brain parenchyma is a hallmark of Alzheimer's disease (AD), but a mechanistic understanding of the role Aβ plays in AD has remained unclear. One important reason could be the limitations of current tools to size and count Aβ fibrils in real time. Conventional techniques from molecular biology largely use ensemble averaging; some microscopy analyses have been reported but suffer from low throughput. Nanoparticle tracking analysis is an alternative approach developed in the past decade for sizing and counting particles according to their Brownian motion; however, it is limited in sensitivity to polydisperse solutions because it uses only one laser. More recently, multispectral nanoparticle tracking analysis (MNTA) was introduced to address this limitation; it uses three visible wavelengths to quantitate heterogeneous particle distributions. Here, we used MNTA as a label-free technique to characterize the in vitro kinetics of Aβ_{1-42} aggregation by measuring the size distributions of aggregates during self-assembly. Our results show that this technology can monitor the aggregation of 10^6–10^8 particles/mL with a temporal resolution between 15 and 30 min. We corroborated this method with the fluorescent Thioflavin-T assay and transmission electron microscopy (TEM), showing good agreement between the techniques (Pearson's $r = 0.821$, $P < 0.0001$). We also used fluorescent gating to examine the effect of ThT on the aggregate size distribution. Finally, the biological relevance was demonstrated via fibril modulation in the presence of a polyphenolic Aβ disruptor. In summary, this approach measures Aβ assembly similar to ensemble-type measurements but with per-fibril resolution.

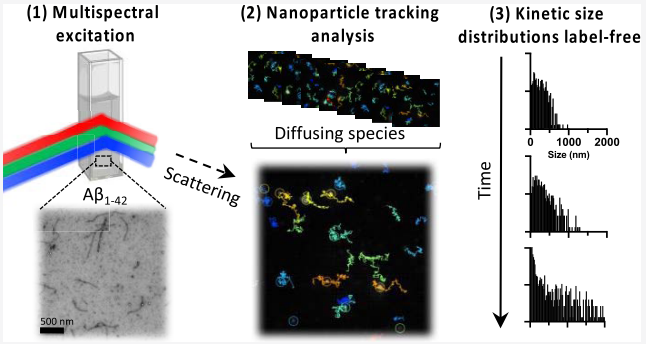

Multispectral nanoparticle tracking analysis (MNTA) was recently introduced as a benchtop tool for quantifying particle size distributions in real time.[1] This optical technique is analogous to dynamic light scattering (DLS) and nanoparticle tracking analysis (NTA) for measuring nano-/microscale particles but offers improved capacity to track polydisperse and fluorescent suspensions. It has previously been demonstrated with various inorganic materials, but investigations in the bioanalytical space have not been reported.[2,3] Amyloid-β (Aβ) is a notorious peptide that exhibits complex pathways of aggregation and self-assembly in physiological conditions. Self-assembling amyloid structures have long been shown to present concurrently with AD and related dementias, but it remains controversial whether they have a causative or simply correlative role. Numerous drugs have shown preclinical benefit (e.g., crenezumab) but failed in Phase III trials.[4−6] While this may be because Aβ is not fundamentally causative of AD, it may also be because techniques for evaluating the mechanism and rates by which Aβ self-assembles are inadequate. There is currently no single tool to quantitatively monitor its oligomerization/aggregation in real time, in solution phase, and with per-fibril resolution of hundreds of fibrils.

Amyloidogenesis is a complex process that is still not fully elucidated—it is generally established that Aβ self-assembly follows a pathway from monomeric species (~4 kDa), to low-molecular-weight oligomers, to nuclei, to high-molecular-weight oligomers, to intermediates, to fibrils. These species vary in size and toxicity and are known to interconvert; furthermore, many different morphologies or subspecies have been reported (e.g., protofibrils, amylospheroids, amyloid-derived diffusible ligands, globulomers, etc.). The major components of Aβ plaques are Aβ_{1-40} and Aβ_{1-42}: these refer to two isoforms of the protein, 40 and 42 residues in length, respectively. Aβ_{1-42} is typically associated with early-stage nucleation and the formation of insoluble fibrils, while Aβ_{1-40} is more soluble and the primary form present in plasma and cerebrospinal fluid (CSF).[7]

Received: March 9, 2020
Accepted: August 7, 2020
Published: August 7, 2020

https://dx.doi.org/10.1021/acs.analchem.0c01048
Anal. Chem. 2020, 92, 11590–11599

Many in vitro techniques have been utilized to study the formation of Aβ fibrils and transient intermediates.[8] Typically, these methods are conducted in parallel because they face various drawbacks when used alone. These can generally be divided into bulk (ensemble) and single-particle techniques. Briefly, ensemble measurements include electrophoresis/western blotting, size exclusion chromatography, light scattering (DLS, MALS), fluorescence assays (via thioflavin-T (ThT) or Congo Red), fluorescence correlation spectroscopy, dot blotting, mass spectrometry, and enzyme-linked immunosorbent assay (ELISA).[8] The most common single-particle techniques are transmission electron microscopy (TEM) and atomic force microscopy (AFM).[9] ELISA and gel electrophoresis can quantitate the bulk load of Aβ in various bodily fluids, and immunostaining can quantitate the location of Aβ fibrils in excised tissues.[10] However, these are both static techniques that inherently only study a single sample or series of samples: ELISA, gels, and immunostaining cannot monitor changes in a sample longitudinally.[11] The ThT assay can monitor the kinetics of Aβ fibril formation, but it does not provide size information.[12] TEM and Cryo-EM offer outstanding spatial resolution but are limited to viewing only a few species at a time.[13−16] Conventional light scattering techniques, such as DLS or multiangle light scattering (MALS), suffer from the exponential dependence of scattering on particle/aggregate size, making it difficult to detect smaller species when large aggregates are present.[17−19] Total internal reflectance microscopy is another important analytical technique that has been used to monitor individual Aβ fibril aggregation in real time.[20,21] While powerful, it is limited in throughput—it selectively monitors only those fibrils in contact with the surfaces of quartz slides and with a limited depth of penetration (150 nm) from the excitatory evanescent field. It also requires the use of ThT or other amyloid-binding dyes.

The working mechanism of MNTA is similar to DLS and NTA (i.e., nanosight[22])—it measures the Brownian motion of particles via scattered light to deduce their size according to the Stokes−Einstein relation. Briefly, a multispectral light sheet illuminates a continuously changing ∼2.5 nL volume, from which suspended particles scatter incident light upon a charge-coupled device (CCD) photodetector. These profiles of scattered light are tracked and recorded to calculate particle size via rate of diffusion. The particle number concentration can be determined by the number of scatterers and the illumination volume. The benefits of monospectral nanoparticle tracking analysis for Aβ characterization have previously been studied by Yang et al.[23] However, DLS and existing NTA rely upon a single-wavelength light source (e.g., 633 nm), while MNTA integrates excitation from three sources (450, 520, 650 nm). This addresses an error source in monospectral techniques—the 6th-power dependence of Rayleigh scattering intensity (at a particular wavelength) on particle size.[24] Larger particles have nonlinear dependence of scattering cross section on particle size predicted by the Mie theory.[25] For both DLS and NTA, this means that in highly polydisperse solutions (such as Aβ), even negligible amounts of large aggregates can completely obscure the scattered intensity from smaller (5−50 nm) species.[18] In some applications, such as antibody production quality control, this fact is leveraged for detecting trace amounts of aggregates nonquantitatively.[26] For NTA, the masking effect of larger particles over smaller ones has been well documented: Tian et al. could not achieve simultaneous measurement of 100 and 1000 nm bead mixtures or 100 and 300 nm bead mixtures,[27] and in mixtures of 100 and 200 nm beads, Krueger et al. observed a clear bias toward the larger species at all tested ratios.[28] In 2018, McElfresh et al. demonstrated that MNTA could address this limitation and accurately measured multimodal mixtures of gold and polystyrene latex particles.[1] One unresolved question was its utility for soft materials—especially those that undergo size dynamics such as aggregating proteins. Here, we evaluated MNTA as a new tool for benchtop characterization of $A\beta_{1-42}$ aggregation—a notoriously arduous and time-consuming task in the AD research community.[8,29,30]

EXPERIMENTAL SECTION

Materials. The following reagents were acquired and used as received: Tris base (Sigma-Aldrich), ammonium hydroxide (28−30%, VWR International), sodium chloride (Sigma-Aldrich), dimethyl sulfoxide (DMSO, Sigma-Aldrich), thioflavin-T (Sigma-Aldrich), $A\beta_{1-42}$ (lyophilized 0.1 mg ea, BACHEM), epigallocatechin gallate (Sigma-Aldrich), 2% uranyl acetate (Electron Microscopy Sciences), gold nanospheres (50 nm, 2 mM citrate, Nanocomposix), silver nanospheres (100 nm, 2 mM citrate, Nanocomposix), polystyrene latex spheres (460 nm: Sigma-Aldrich, 90 nm/490 nm/1000 nm: Ted Pella), and Type 1 Reference Water (XZero).

Preparation and Storage of $A\beta_{1-42}$. As-purchased $A\beta_{1-42}$ peptide was stored at −20 °C and aliquoted using 10% (v/v) NH_4OH. Briefly, 0.1 mg of peptide was resuspended in NH_4OH to a concentration of 0.5 mg/mL. The sample was then split into aliquots containing 0.025 mg each and lyophilized using a LabConco FreeZone (2.5 L). These samples were stored at −80 °C prior to use.

Aggregation of $A\beta_{1-42}$ Peptide and Fluorescent Monitoring. Aliquots were first solubilized in DMSO to a concentration of 500 μM and sonicated for 5 min to minimize preformed aggregates. The aliquots were then diluted to a concentration of 5 μM in 40 mM Tris buffer (pH 8.0) and 150 mM NaCl to initiate aggregation. Aggregation was monitored using the fluorescent molecule Thioflavin-T (ThT). This molecule is a benzothiazole dye commonly used to monitor Aβ aggregation—it binds specifically to β-sheet structures to yield enhanced fluorescence at 485 nm. For fluorescent detection, Aβ samples were incubated with 10 μM ThT in 96-well plates and monitored with a Molecular Devices SpectraMax M5 spectrophotometer. Fluorescence measurements were recorded every 5 min (ex: 440 nm, em: 485 nm).

Modulation of $A\beta_{1-42}$ Aggregation With Epigallocatechin Gallate (EGCG). Stock solutions of EGCG were prepared at 20 mM in DMSO. EGCG was added to fibrillous $A\beta_{1-42}$ samples (after 12 h of aggregation as described above) for a final concentration of 50 μM EGCG. These samples were incubated for 24 h at room temperature before characterizing with fluorescence measurements, MNTA, and TEM.

Transmission Electron Microscopy. Carbon/Formvar grids (300 mesh, Ted Pella Inc.) were first exposed under a UV lamp for 1 h to increase surface hydrophilicity. Five microlitres of 5 μM Aβ (40 mM Tris, 150 mM NaCl) was drop cast on a grid and allowed to settle for 1 min. A wedge of a filter paper was applied at a right angle to the drop and used to wick away the sample. Five microlitres of DI water was added to the grid and removed as before after 1 min. Five microlitres of uranyl

https://dx.doi.org/10.1021/acs.analchem.0c01048
Anal. Chem. 2020, 92, 11590−11599

acetate (2%) was then applied and allowed to stain for 30 s before removal as before. Imaging was performed with a JEOL 1200 EX II TEM at 80 kV and micrographs were captured with a 2K X2 KGatan CCD camera.

MNTA Measurements. MNTA measurements were conducted using a commercially available ViewSizer 3000 from Horiba Scientific (Irvine, CA) at 27 °C. Details of this system have been described previously but are briefly summarized below.[1] For all Aβ measurements, the instrument settings were as follows: 15 ms exposure, 24 dB gain, 70 mW blue laser power, 12 mW green laser power, and 8 mW red laser power. Incident light from these sources is scattered by the sample and photons are sorted by wavelength with a Bayer filter and detected with a CCD photodetector. In this way, each channel of light is recorded by distinct pixels of the CCD. Each of these channels is then separated to form grayscale images comprised of the scattered light profiles (i.e., spots/blobs) from the particles in the excitation field of view (162 μm × 288 μm × 50 μm). Automated noise analysis is performed to determine the optimal wavelength for representing each particle (ensuring optimal scattering for a given particle size), and a final 8-bit composite video is generated for tracking analysis.[1] The system also performs user-definable image thresholding to reduce background noise from the camera. By default, a Gaussian blur filter (to reduce speckling) and 10% noise threshold (expressed as a percentage value of the total number of pixels) are applied such that all pixels below this threshold are set to zero (0−255 range). For measurements with fluorescent gating, the green and red lasers were deactivated, and a 450 nm long-pass filter was inserted between the sample cuvette and detector.

The samples were prepared as described above and used to fill a quartz cuvette cell with a minimum of 0.4 mL. For each sample or time point, 15 videos were recorded at a framerate of 30 fps for 10 s (300 frames per video). Between each video, the samples were stirred at a speed of ∼30 rpm for 5 s with a 5 mm poly(tetrafluoroethylene) (PTFE) stir bar to push a new volume of the sample into the illuminated region. After stirring, the sample was allowed to equilibrate for 10 s to minimize directional flow. Particle detection was initiated according to a user-definable intensity threshold. Here, we used a dynamic detection threshold of 2 standard deviations above the median (e.g., if the median pixel intensity of a frame was 70, and the standard deviation of pixel intensities was 5.1, then the particles with intensities (calculated for a 20 pixel feature diameter) less than 70 + 2 × 5.1, or 80, were not counted). This dynamic threshold is more robust for the polydisperse samples than a constant minimum intensity as it accounts for the total frame intensity.[31] For each video, time-resolved particle coordinates were acquired by determination of the radial symmetry centers.[32]

Mathematically, the calculated diffusion coefficient (and hydrodynamic diameter) is extracted from the optimized least-squares fit (OLSF) of the mean-squared displacement (MSD) curve for a given particle track. However, it has been established that the finite length of a single-particle trajectory highly influences the MSD fit:[33] For large time lags, the increased variance and correlated values of the MSD can significantly contribute to error; for short time lags, the MSD variance is heavily affected by dynamic localization error and motion blur.[34,35] To address these issues, MNTA applies Cramér−Rao statistics to optimize the least-squares fit of the MSD on a track by track basis: The system ignores the track or calculates the hydrodynamic diameter according to the relative uncertainty on D (mathematically expressed in detail by Michalet et al.).[36] Specifically, a maximum threshold value of 0.4 for the relative uncertainty was used. Further tracking parameters were as follows: The maximum jump distance was 20 pixels, the minimum number of frames for tracking analysis was 5, and the maximum number of frames a particle could be lost before ending a track was 2. These are factory set but adjustable values for the system. The extraction of particle size is as follows: First, the mean-squared displacement (MSD) is calculated from the time-resolved coordinates of each particle x_i and y_i over N frames according to eq 1.

$$\mathrm{MSD}(n) = \frac{1}{N-n}\sum_{i=1}^{N-n}(x_{i+n} - x_i)^2 + (y_{i+n} - y_i)^2 \quad (1)$$

From the MSD for a given particle, the diffusion coefficient D is determined using the time delay between frames Δt and an optimized least-squares fit of the MSD as a function of n (eq 2).[1]

$$\mathrm{MSD}(n) = (4\Delta t D)n \quad (2)$$

The hydrodynamic diameter d_H is then calculated according to the Stokes−Einstein equation (eq 3). Here, k_B is the Boltzmann constant, T is temperature, and η is the solvent viscosity.

$$d_H = \frac{k_B T}{3\pi\eta D} \quad (3)$$

RESULTS AND DISCUSSION

Application of MNTA to Concentration and Size Measurements of Inorganic Nanoparticles. Inorganic nanoparticles and solution phase aggregates of Aβ_{1-42} were quantified using MNTA with a commercially available system from Horiba Scientific illustrated and are described in Figure 1. The raw data generated by the instrument comprises a series of videos (∼10 s each) that display the scattered light profiles from particles in solution. The number of videos is defined by the user and is a tradeoff between total acquisition time and total particle counts—we used 15 videos per Aβ sample and

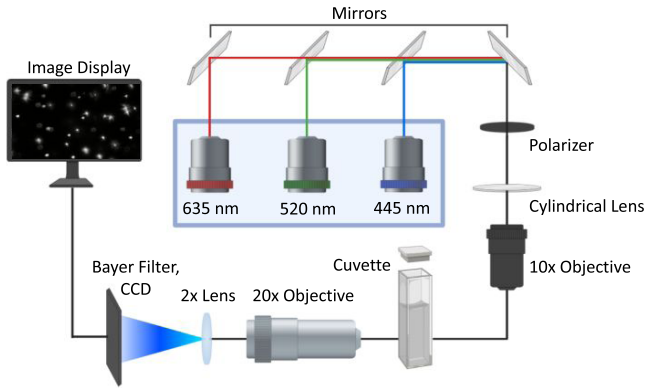

Figure 1. Schematic of MNTA instrumentation. The instrument consists of three individual light sources (635, 520, and 445 nm) with adjustable power levels, dichroic mirrors to form a single sheet of light, a polarizer, a cylindrical lens, a 10× objective lens, a sample cuvette, a 20× objective lens, a 2× lens, a Bayer filter, and a CCD detector for image capture.

https://dx.doi.org/10.1021/acs.analchem.0c01048
Anal. Chem. 2020, 92, 11590−11599

did not observe a significant effect of video number on concentration measurements (Figure S1). Each frame of a video represents a snapshot of the particle positions in a 2.5 nL rectangular volume, i.e., the volume illuminated by the focused light sheet, at a particular time. The positions of the particles are recorded via tracking of the radial centers and used to calculate the size of the particles according to their degree of Brownian motion.[32,36,37]

We first assessed the measurable concentration range of the MNTA system by diluting gold, silver, and polystyrene latex (PSL) spheres across 4 orders of magnitude (Figure 2). We

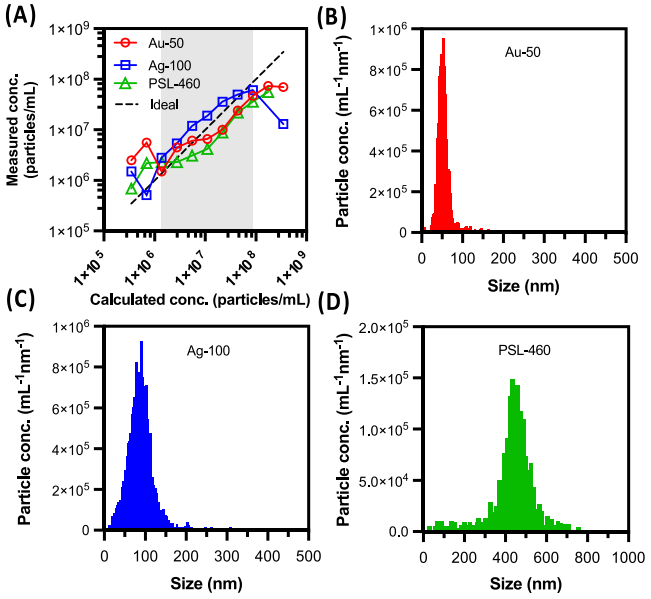

Figure 2. Measurement of inorganic particle concentrations and size distributions using MNTA. (A) Commercial gold nanospheres (2 mM citrate, nominal d = 50 nm), silver nanospheres (2 mM citrate, nominal d = 100 nm), and polystyrene latex spheres (aqueous, nominal d = 460 nm) were diluted in water (XZero Type 1 reference water) across 4 orders of magnitude from their stock concentration (x-axis) provided by the manufacturer. The concentrations measured with MNTA for each dilution were plotted on the y-axis. The dashed line represents an ideal linear relationship for comparison. The shaded region shows the concentrations for which linearity was observed, between 10^6 and 10^8 particles/mL (Au-50: R^2 = 0.9852, Ag-100: R^2 = 0.9926, PSL-460: R^2 = 0.9740). (B–D) The size distributions of the particles in (A) are shown for (B) Au-50, (C) Ag-100, and (D) PSL-460 and are presented at calculated concentrations of 4.4×10^7, 4.4×10^7, and 8.7×10^7 particles/mL, respectively. The recorded sizes were as follows: Au-50 (modal: 50 nm, avg: 59 nm), Ag-100 (modal: 91 nm, avg: 93 nm), and PSL-460 (modal: 437 nm, avg: 457 nm).

assigned the absolute (calculated) concentrations by diluting from the stock values provided by the suppliers. As these are most commonly determined via mass concentrations of the starting material, they are inherently estimates that rely on the perfect uniformity of the particles. Though deviations in the measured concentrations existed on a per-sample basis, we did not observe significant variation in the measurable range across these particle types/sizes, observing a linear trend between 10^6 and 10^8 particles/mL (Figure 2A). Particle size distributions for the gold, silver, and PSL particles are shown in Figure 2B–D to confirm the accuracy of the size measurements.

To understand how MNTA compares to single-wavelength NTA, we investigated particles and mixtures with sizes relevant to Aβ species, particularly from <100 to 1000 nm. Rather than comparison to a commercial single-wavelength system (e.g., NanoSight), we selectively activated/deactivated the component lasers of the MNTA system. This allowed isolation of the effect of wavelength on the results, as all other hardware and processing elements were constant. Acquisition settings for the PSL solutions are detailed in Table S1. In Figure S2, we used MNTA to measure monomodal solutions of nominal 90 nm (row A), 490 nm (row B), and 1000 nm PSL particles (row C) (TEM-standard grade). For each row, panels (i)–(iv) show the raw particle counts for multispectral (i), blue (ii), green (iii), and red (iv) excitation. The shaded regions indicate the median 80% of particle counts (where D10 and D90 are the left and right boundaries, respectively). From these plots, we observe that each of the three particle sizes has an ideal excitation wavelength, as revealed by the spread of the D10–D90 range. For 90 nm particles, the blue wavelength reduces this spread by 34% relative to green and 48% relative to green. For 490 nm particles, the green wavelength is best (23% narrower relative to blue and 14% relative to red), and for 1000 nm particles, the red wavelength is best (41% narrower relative to blue and 28% relative to green). In the case of 90 nm PSL, we also observe a decrease in the total number of particle counts as the excitation wavelength shifts from blue to green to red. This wavelength-dependent scattering is expected from Mie theory. The consequence is that no single wavelength is ideal for all particle sizes that span the nanosize regime.

To investigate this further, we prepared trimodal mixtures of these PSL particles across a full order of magnitude of concentrations (Figure S3). We measured mixtures with relative concentration ratios of 10:5:1 (row A), 1:1:1 (row B), and 1:5:10 (row C) (PSL-90/PSL-490/PSL-1000). Panels (i)–(iv) show the particle counts for multispectral (i), blue (ii), green (iii), and red (iv) excitation. The histograms are presented with the dashed lines to show the nominal diameters for each particle type. In addition, the shaded regions approximate the width of the distribution for each particle type: They were calculated by taking 1 standard deviation above and below the modal size for each type. The standard deviations of the monomodal particle distributions in Figure S2 were used for this purpose. The particle counts in each region were summed to calculate relative concentration ratios. Collectively, the quality of the measurements can be determined by observing the distance of the modal size (highest bin) from the nominal size (dashed line) and by measuring the particle count ratio between the three shaded regions. Panel (v) for each row compares the measured particle ratios vs their theoretical ratio (gray).

It is obvious that the green and red lasers are insufficient for detection of small particles (e.g., 90 nm) when larger species (490 and 1000 nm) are present at comparable concentrations (Figure S3A(iii,iv),B(iii,iv)). Green and red only count 9 and 1%, respectively, of the PSL-90 particles detected with multispectral (RGB) excitation for the 10:5:1 mixture (Figure S3A(i–v)). When comparing RGB excitation to blue-only for the 10:5:1 mixture, we see that RGB is closer to the ideal ratio than blue-only (Figure S3A(v)). However, blue is superior over green and red if only a single wavelength is available. For the 1:1:1 mixture (Figure S3B(i–v)), PSL-90 and PSL-490 are well-accounted for by RGB but PSL-1000 is undercounted (Figure S3B(v)). Blue also undersizes the PSL-90 in this mixture (Figure S3B(ii)). Each configuration had difficulty with the 1:5:10 mixture (Figure S3C(i–v)). This is a

https://dx.doi.org/10.1021/acs.analchem.0c01048
Anal. Chem. 2020, 92, 11590–11599

particularly challenging case due to the high number of intensely scattering large particles, preventing good resolution of the 90 nm population even for the RGB configuration. We conclude that RGB excitation is well-suited for the polydisperse mixtures over single-wavelength excitation especially for mixtures that are either skewed toward smaller particles in number or evenly distributed.

In NTA, one important parameter is the max jump distance (MJD). During analysis of the recorded videos, the processing algorithm compares the positions of the particles in one frame to the subsequent frame to construct tracks of finite length. The MJD is a threshold distance—if a particle is found in a successive frame within the MJD from a particle in the previous frame, then a track segment is formed. The track continues to grow until no particle is found within the MJD of a successive frame, or until multiple particles are found within the MJD, thereby terminating the track. Ideally, the MJD should be set unique to each population size. This is obviously quite difficult during dynamic experiments such as amyloid aggregation where the samples are not only polydisperse but also changing dynamically. In lieu of this, the MJD should at least be set such that it does not exclude small particles that diffuse at a higher rate than larger particles. We performed MNTA measurements on three small nanoparticle standards (50, 90, and 100 nm) across a range of MJDs and plotted the particle counts with respect to the MJD (Figure S4). From this data, we observed that a MJD of 20 pixels was sufficient for measuring 97 ± 2% of particles present in the 50−100 nm size range, a reasonable lower range of confidence. Therefore, we used a MJD of 20 for Aβ measurements.

Real-Time Monitoring of Aβ_{1-42} Aggregates. The solid Aβ_{1-42} peptide was pretreated and individually aliquoted using 10% NH_4OH followed by lyophilization to minimize initial aggregation.[38] To illustrate the raw data from Aβ_{1-42} as visualized by MNTA, Figure S5 first compares the initial video frame of recorded data from aggregation buffer before (Figure S5A) and after (Figure S5B) the addition of Aβ_{1-42} (Figure S6 for distributions). It then shows the conversion to 8-bit data (Figure S5C) that is used for particle tracking (Figure S5D−G). Using MNTA, we found that upon resolubilization in buffer (40 mM Tris, 150 mM NaCl, pH 8.0), these Aβ_{1-42} aliquots already contained some intermediates with an average size of 160 ± 10 nm (±standard deviation of n = 4 replicate means). This is indicative of the high instability of the Aβ_{1-42} peptide and reflects prior reports.[39,40] For a given sample, we routinely observed increases in the average size and standard deviation (i.e., polydispersity) of the aggregate distribution over the course of measurement (12 h, 30 min intervals).

The viscosity of the sample changes as a function of protein concentration, and the viscosity is a key parameter in the Stokes−Einstein relationship.[41] To account for the different viscosity of the protein solutions relative to water,[42,43] we adapted a simple protocol that has been previously demonstrated using DLS.[44] We validated the extension of this technique to MNTA by comparing viscosity measurements of aqueous glycerol solutions to their known theoretical values (Figure S7). We observed a linear correlation (R^2 = 0.9544) between theoretical viscosities of glycerol−water mixtures and MNTA-measured viscosities. We used the same protocol for measuring the viscosity of aqueous Aβ. This first entailed measuring the size distribution of a stock sample of polystyrene latex spheres (nominal diameter 90 nm) at a high concentration in water. The particles were then measured at the same concentration in 5 μM Aβ. This resulted in average measured diameters of 84 nm (d_1) in water and 161 nm (d_2) in 5 μM Aβ (Figure S8). Therefore, the viscosity of the Aβ solution was calculated according to $\eta = (d_2/d_1) \times \eta_{H_2O,27C}$ = (161 nm/84 nm) × 0.85 cP = 1.63 cP. This value was used for processing all Aβ aggregation experiments.

Representative data generated from a single sample monitored with MNTA is shown in Figure 3. To aid in distinguishing changes in the size distribution, we defined a minimum size threshold for aggregation as the largest particle detected by the t = 0 h MNTA measurement (Figure 3A, red dashed line). Therefore, each sample served as its own control and baseline for aggregation. Particle size distributions were collected every half hour but are visualized at 3 time points of growth (t = 0, 2, 4 h) to demonstrate the widening of the size distribution and the number increase in larger aggregates (particles >690 nm for this sample) during the growth phase. The aggregate counts have units of mL^{-1} nm^{-1} because they are grouped as a histogram of bins with 20 nm widths—each bar corresponds to the concentration of aggregates in that particular bin.

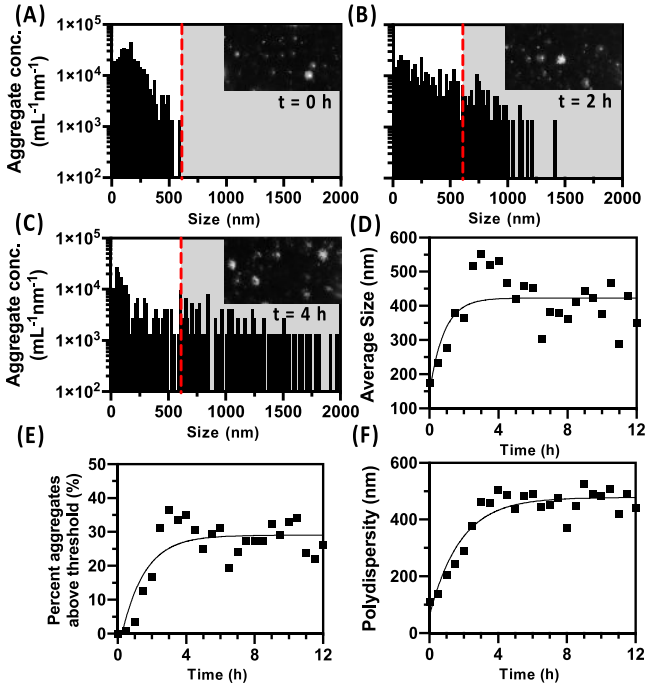

Figure 3. Particle size distributions and growth trends from a single aggregation experiment using MNTA. (A−D) Aβ_{1-42} was incubated in Tris (40 mM, 150 mM NaCl, pH 8.0) and measured every hour. Particle size distributions recorded at (A) 0, (B) 2, and (C) 4 h. The red plane indicates the size of the largest aggregate detected at t = 0 h. Pre-grayscale video frames taken from the first frame of each raw video file are presented in the insets, showing the scattered light from individual aggregates at each time point. (D) Average size of aggregates in solution plotted against time for a representative aggregation experiment indicates fibril growth. (E) Total percentage of measured aggregates above the t = 0 state (red line) can also be plotted over time as an alternative metric of growth. (F) Standard deviation of the particle size distribution (i.e., the polydispersity) shows the spreading of the distribution over 4 h followed by an equilibrium state matching the size trend. Kinetic data in (D−F) are presented with a least-squares one-phase association fit.

https://dx.doi.org/10.1021/acs.analchem.0c01048
Anal. Chem. 2020, 92, 11590−11599

The average sizes (±standard deviations of the size distributions) measured for panels A−C were 180 ± 110 nm (0 h), 360 nm ± 290 (2 h), and 530 nm ± 500 nm (4 h). Here, the standard deviations provide the simplest metric for quantifying the spread of the size distributions. We use them as convenient surrogate values for the polydispersity of the solutions and for observing kinetic changes in the polydispersity. Since the size distributions are not normal, Chebyshev's theorem can be a useful rule of thumb: at least 75% of the measured aggregates lie within 2 standard deviations of the mean (this is overly conservative as sizes cannot be ≤0). While D10, D50, and D90 values offer a more rigorous description of particle size distributions, standard deviations were suitable for our kinetic analysis.

In addition to Brownian motion-based sizing, the real-time display of scattered light from the samples provides a qualitative confirmation of aggregation via increased scattering intensity on a per-particle basis, shown as still frames from the raw videos in the upper right of Figure 3A−C. Figure 3D shows the trend in average Aβ_{1-42} aggregate size for the same sample every 30 min, which indicated that the majority of growth occurred during the first 4 h and reached an equilibrium after this point. The extent of aggregation could also be visualized and quantified according to the percentage of total aggregates larger than the maximum size measured in the initial state (Figure 3E). Figure 3E shows that this value plateaued after reaching a value of ∼29% over 4 h incubation. Third, the polydispersity of the size distribution, as represented by its standard deviation (Figure 3F), followed the same trend.

Comparison of MNTA to ThT Assay and TEM. To validate the kinetic trends of native Aβ_{1-42} acquired with MNTA and assess reproducibility, we measured aggregate size distributions across four replicates in parallel with the fluorescence ThT assay (ex: 440 nm, em: 485 nm): The average size trend measured by MNTA was positively correlated with ThT fluorescence when the techniques were conducted simultaneously (Pearson's r = 0.821, P < 0.0001; Figure 4A). Size distributions from the individual replicates are presented in Figure S9. The relative standard deviation in measurement over this time course ranged from 7 to 44% for MNTA and 6 to 48% for ThT fluorescence. On average, we measured 100% growth in average size and a 320% increase in raw ThT fluorescence over the first 4 h of incubation. These values did not significantly change by the 12 h time points. We observed that average size fluctuations between 300 and 400 nm were not matched by differences in ThT fluorescence on a per-time-point basis (Figure 4A). This could suggest dynamic coalescence/decoupling without changes in total β-sheet content, but we also cannot rule out sampling bias in the MNTA technique relative to the ensemble average of whole sample fluorescence. On average, the polydispersity increased with the same trend as the average size (Figure 4B). We also observed a linear decrease of 40% (nonzero slope, P < 0.0001) in total aggregate concentration from 5.4 × 10^6 to 3.2 × 10^6 mL^{-1} over the 12 h measured (Figure 4C). This could be due to the gradual integration of smaller species into larger aggregates, resulting in a lower total aggregate concentration. Over the course of the measurement period, it is also likely that the largest fibrils sediment below the illuminated volume and are not resampled. Regardless, even if sampled, we note that the processing used for nanoparticle tracking analysis cannot be used to measure multiple-micron-sized particles (e.g., >2 μm), as their MSD vs Δt will not obey a linear fit.

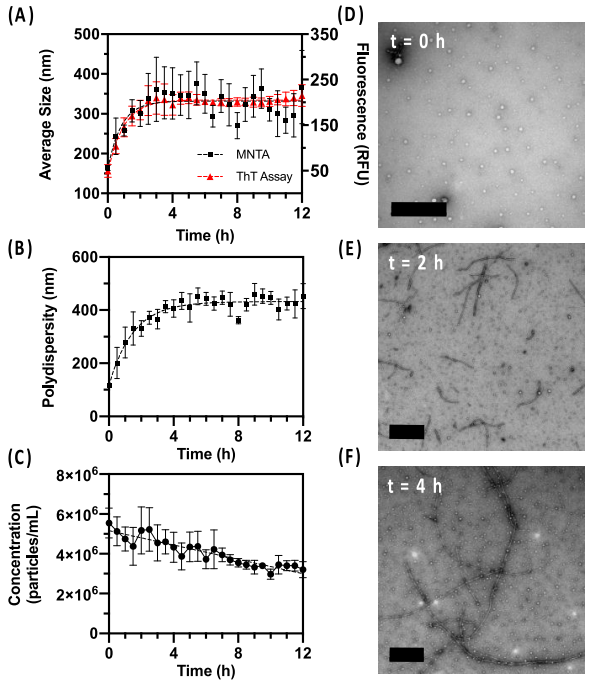

Figure 4. Averaged kinetic trends of Aβ_{1-42} aggregation using MNTA in tandem with the fluorescence ThT assay and TEM. (A) Kinetics of aggregation are plotted via average size using MNTA and fluorescence using the ThT assay. MNTA size kinetics are correlated to the gold standard ThT fluorescence assay (Pearson's r = 0.821, P < 0.0001). Error bars = SEM, n = 4 replicates. (B) Average polydispersity of the size distributions measured hourly indicates widening of the size distributions until a plateau at 4−5 h. Error bars = SEM, n = 4. (C) Concentration of aggregates (0−2 μm range) measured via MNTA decreases over time. R^2 = 0.851, error bars = SEM, n = 4. (D−F) TEM images at T = 0, 2, and 4 h reveal formation of mature fibrils. Scale bars = 500 nm.

To further validate the accuracy of monitoring aggregation with MNTA, we imaged the Aβ_{1-42} at various time points using TEM. Representative images are shown at t = 0 h, t = 2 h, and t = 4 h (Figure 4D−F). We observed spherical intermediates and potentially oligomeric species at t = 0 h that grew into large micron-scale fibrils after 4 h. The sizes were not quantitatively estimated from TEM images due to the significant heterogeneity of Aβ_{1-42} fibrils and difficulty in distinguishing individual species; however, fibrillary growth was observed similar to prior work.[45] TEM showed no further growth beyond 4 h, which is consistent with the plateau in size and fluorescence observed at 4 h with MNTA and the ThT assay, respectively.

MNTA Measurements of Aβ_{1-42} Fibrillation With Fluorescent Gating. ThT binds specifically to the β-sheet regions that form during Aβ aggregation, and the ThT assay is a workhorse in Alzheimer's disease research. ThT has no fluorescence signal when unbound but produces fluorescence when bound to Aβ (excitation at ∼485 nm; Figure 5A). Thus, we evaluated the use of MNTA with and without the addition of ThT. MNTA can be performed using light scattering as described, but light emitted by the fluorescent samples can also be isolated and used for tracking by placing an optical filter between the sample and detector. We used MNTA with and without fluorescent gating to distinguish two types of signal: (1) scattered excitation light and (2) fluorescence from ThT bound to Aβ. Figure 5B shows an Aβ_{1-42} solution that does not

https://dx.doi.org/10.1021/acs.analchem.0c01048
Anal. Chem. 2020, 92, 11590−11599

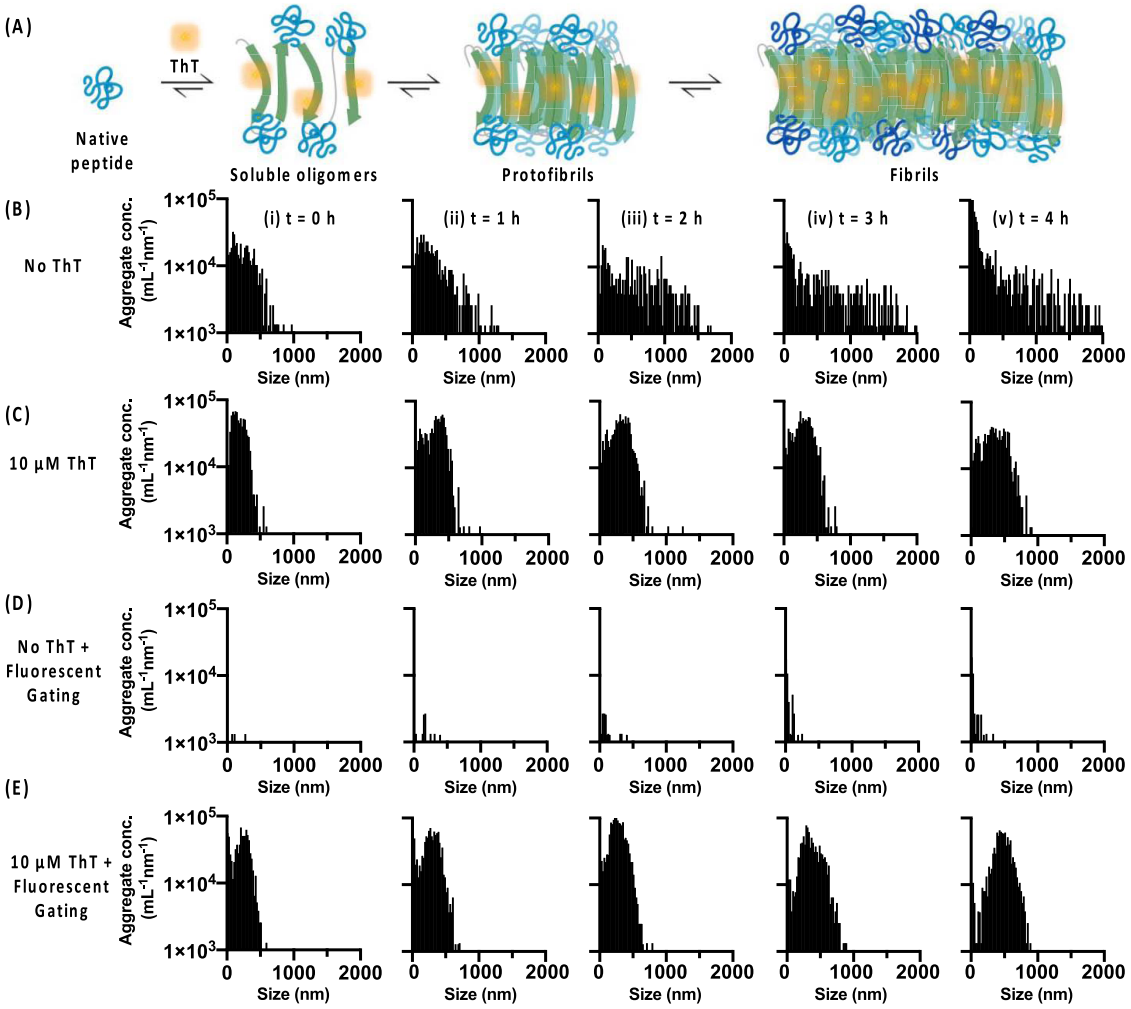

Figure 5. MNTA with and without fluorescence gating and the effects of ThT on Aβ_{1-42} size distributions. (A) Schematic of the ThT−Aβ interaction. ThT selectively binds β-sheet motifs that form during oligomerization and fibrillation. This decreases the nonradiative rate of decay of the fluorophore and activates its fluorescence. (B) Size distributions measured without ThT using NTA mode (all three lasers, no filter) from t = 0−4 h. (C) Aβ size distributions measured with 10 μM ThT using NTA mode from t = 0−4 h. (D) Aβ size distributions measured without ThT using fluorescent gating (only 445 nm laser activated with a 450 nm long-pass filter for the removal of nonfluorescent/scattered light) from t = 0−4 h. (E) Aβ size distributions measured with 10 μM ThT using fluorescent gating from t = 0−4 h.

contain ThT monitored for 4 h. The same solution was measured in parallel with fluorescent gating (Figure 5D), which entailed deactivation of the red and green lasers while maintaining the blue (445 nm) and inserting a 450 nm long-pass filter between the sample and detector. The blue excitation was chosen to most closely match the absorbance maximum of ThT (440 nm). Here, the total number of raw particle counts detected over the course of measurement was 20 times lower (97 vs 2186) than without fluorescent gating. This is because no fluorescent light was produced by the Aβ_{1-42}, and the scattered excitation light was removed by the filter. In contrast, when the same sample was incubated with 10 μM ThT, the aggregates were obvious both with (Figure 5E) and without fluorescent gating (Figure 5C). For the samples that contained ThT (Figure 5C,E), we observed a larger average size with fluorescent gating than without after 4 h (470 ± 160 nm vs 360 ± 180 nm)—this was supported by the lower number of smaller aggregates detected in the fluorescence-gated sample. The modal size of the fluorescence-gated sample was 440 nm, while the nongated sample was 30 nm after 4 h. This difference supports the hypothesis that after fluorescent gating, detection was selective toward aggregates with more bound ThT, i.e., larger species with higher β-sheet content.

Perhaps more notably, we observed a significantly different shape of the size distribution between Aβ_{1-42} incubated with (Figure 5C) and without (Figure 5B) ThT. Although the average sizes of these two samples were comparable (360 nm vs 410 nm), the standard deviations of these distributions were 180 and 480 nm, respectively. To further examine this effect, we allowed Aβ_{1-42} to aggregate and added ThT after 4 h had elapsed (Figure S10). We did not observe the same shift in the distribution as when it was present throughout the measurement though an increased number of particles were detected in the 500−1500 nm range. This could be due to the addition of ThT fluorescence to the scattered light already produced by each aggregate effectively increasing the sensitivity to the fibrils with bound ThT. These observations collectively suggest that ThT could play an interfering role, though minor, in the formation or stability of certain Aβ species—an idea that has been suggested previously in the literature.[12,46] A full investigation of the ThT−Aβ interaction is beyond the scope of this work, but our data indicate the potential utility of

https://dx.doi.org/10.1021/acs.analchem.0c01048
Anal. Chem. 2020, 92, 11590−11599

MNTA for the mechanistic studies of aggregation-sensitive dyes. Importantly, as a tool for monitoring the raw aggregation state of peptides/proteins, MNTA does not require the use of exogenous dyes, and we consider this label-free sensing a notable advantage of the technique.

MNTA for Monitoring Potential Inhibitors of Aβ_{1-42} Fibrillation. To evaluate the ability to measure small-molecule-based alterations in Aβ_{1-42} fibrillation with MNTA, we incubated the samples with a naturally produced polyphenol with previously reported activity against Aβ aggregation for 24 h: epigallocatechin gallate (EGCG).[47−49] Figure 6A,B shows a typical size distribution after 12 h

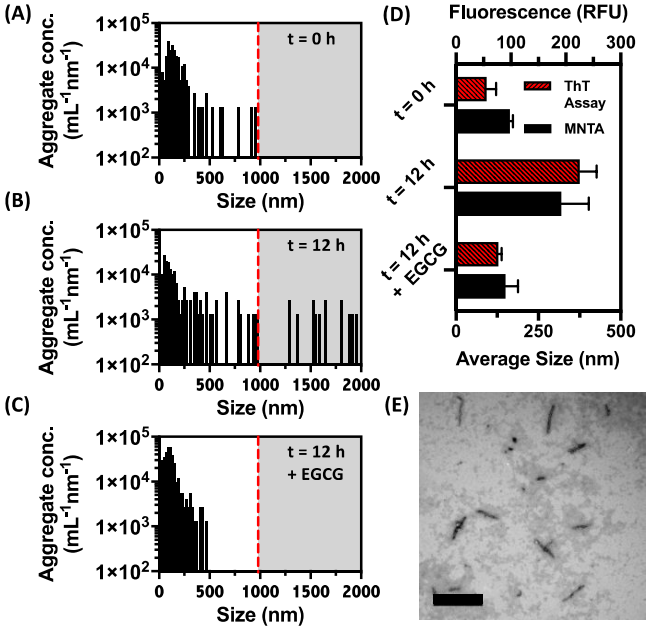

Figure 6. Modulation of the Aβ_{1-42} fibrils using a previously reported disruptor of aggregation can be monitored with MNTA. (A−C) Particle size distributions recorded at (A) 0 h and (B) 12 h for 5 μM Aβ_{1-42}, followed by (C) 24 h incubation in EGCG at 37 °C. The red line indicates the size of the largest aggregate detected at t = 0 h. (D) Fluorescence measured via ThT assay and average size measured via MNTA are shown before (t = 0 h: 160 ± 8.7 nm, 56.0 ± 23.9 RFU) and after aggregation (t = 12 h: 320 ± 83 nm, 226 ± 42.8 RFU) followed by 24 h EGCG incubation (t = 12 h + EGCG: 150 ± 38 nm, 77.5 ± 7.89 RFU). Error bars = SEM, n = 3. (E) TEM of the Aβ_{1-42} aggregates after EGCG incubation reveals intermediate-sized species. Scale bars = 500 nm.

followed by its shift toward the initial state after 24 h EGCG incubation (Figure 6C). In this sample, no aggregates were observed above the t = 0 h threshold following EGCG incubation. By averaging three replicates, the total concentration of aggregates transitioned from 2.8 × 10^6 mL^{-1} (t = 0 h) to 6.3 × 10^5 mL^{-1} (t = 12 h) to 2.2 × 10^6 mL^{-1} (t = 12 h + 24 h EGCG). We conducted these experiments in parallel with the ThT assay (Figure 6D) and observed a correlation between the average sizes measured with MNTA and ThT fluorescence. This suggested that the fluorescence reduction related to the reduction in aggregate size and reinforced the notion that MNTA could monitor Aβ_{1-42} disruption without an exogenous dye. Finally, we used TEM as secondary confirmation of Aβ_{1-42} remodeling via EGCG: Figure 6E shows a TEM image of the mature Aβ_{1-42} fibrils (12 h growth) after they have been incubated with EGCG for 24 h. These aggregates resemble the intermediate species observed during the growth stages of fibrillation rather than the extensive and filamentous network of the mature fibrils associated with complete aggregation.

Practical Considerations and Limitations. The emphasis of this first work on MNTA for Aβ aggregation is its utility for label-free kinetic monitoring and aggregate counting in solution phase with the potential for size-based analysis. Hydrodynamic diameters were calculated according to the Stokes−Einstein relation. Therefore, average sizes reported represent spheres of equal diffusion coefficients. For this reason, high-resolution imaging techniques such as TEM and AFM remain the most accurate choices for morphological characterization of the aggregates and fibrils. Nevertheless, more sophisticated hydrodynamic models could be implemented in future work that account for dynamic viscosities and rod/fibrillous particle dimensions.[50]

The lower size limit of detection for a particle is governed both by its scattering cross section and the sensitivity of the optics (e.g., camera gain, exposure time, and laser power). In this work, we used laser power settings optimized for polydisperse solutions (where power increases from red, to green, to blue to compensate for differential scattering) and factory-default camera settings for all Aβ experiments. 2% of all Aβ aggregates we detected were in the 0−10 nm binwidth. The manufacturer quotes a lower limit of 10 nm, which is roughly the same as commercial NanoSight. The upper size limit of measurement occurs near the point at which sedimentation begins to dominate over diffusion. This is both material specific (density) and governed by the resolution of the camera, as even sinking particles experience Brownian motion that is detectable with high enough resolution. In ambient aqueous conditions, the root-mean-square-displacement (L) for a 1500 nm particle in the MNTA system is 1 pixel. This is the distance the particle can be predicted to travel between frames. For a 2000 nm particle, L = 0.9 pixels. Therefore, error will begin to be introduced into the MSD fitting for particles above 1500 nm, and the upper limit of accuracy lies in this range. Since the presence of larger aggregates was still of interest to us, we set the upper bound for analysis at 2000 nm (note: NTA also conventionally uses 2000 nm as an upper limit for analysis).[51] For concentration measurements, we found that MNTA provided reasonable values within 2 orders of magnitude (~10^6−10^8 particles/mL for Au/Ag/PSL nanospheres). The upper concentration limit is constrained by the overlapping scattering profiles that cannot be distinguished by particle-tracking algorithms; the lower limit is due to the distance between the suspended particles exceeding the illuminated field of view. In the future, implementation of a recently developed modified displacement probability model could improve the upper concentration limit.[52]

To mitigate against potential selection bias from the small sampled volume (2.5 nL × n videos), a higher number of videos can be recorded. The same strategy can be applied for lowering the concentration limit of detection, which is on the order of 10^6 particles/mL for inorganic nanoparticles. However, this should be weighed against the increased measurement time and frequency of sample stirring, which can interfere with unstable samples such as aggregating proteins. Despite these considerations, our data suggests that MNTA is a promising benchtop tool for studying the aggregation states of the Aβ peptide, especially when compared

https://dx.doi.org/10.1021/acs.analchem.0c01048
Anal. Chem. 2020, 92, 11590−11599

to monospectral light scattering techniques that are limited in their resolving power of polydisperse solutions.

CONCLUSIONS

This work reports the first application of multispectral nanoparticle tracking analysis to the characterization of Aβ aggregation. We determined that it could monitor the dynamics of Aβ_{1-42} aggregate size distributions longitudinally and label free via kinetic correlation with the ubiquitous ThT assay. In addition, fluorescently tagged aggregates could be selectively measured by utilizing an appropriate excitation laser and filter. Simultaneous measurement via ThT fluorescence and TEM also suggests that MNTA is suitable for assessing potential disruptors of Aβ_{1-42} fibrillation. The benchtop measurement takes between 15 and 30 min for analysis and processing while achieving real-time analysis of hundreds of fibrils per imaging event.

ASSOCIATED CONTENT

Supporting Information

The Supporting Information is available free of charge at https://pubs.acs.org/doi/10.1021/acs.analchem.0c01048.

Acquisition settings for PSL particle measurements (Table S1); effect of video number on total measured aggregate concentration (Figure S1); multispectral vs monospectral excitation for NTA of monomodal PSL (Figure S2) and trimodal PSL (Figure S3); detection of the small nanoparticles as a function of max jump distance (Figure S4); principle of MNTA for Aβ sizing via Brownian dynamics (Figure S5); comparison of the measured size distribution for buffer before and after addition of Aβ (Figure S6); evaluation of viscosity measurements using MNTA (Figure S7); determination of viscosity of Aβ solutions using MNTA (Figure S8); individual replicates for all aggregation experiments (Figure S9); effect of ThT on the Aβ size distribution after aggregation has already proceeded (Figure S10) (PDF)

AUTHOR INFORMATION

Corresponding Author

Jesse V. Jokerst − *Department of NanoEngineering, Materials Science and Engineering Program, and Department of Radiology, University of California, San Diego, La Jolla, California 92093, United States;* orcid.org/0000-0003-2829-6408; Email: jjokerst@eng.ucsd.edu

Authors

Colman Moore − *Department of NanoEngineering, University of California, San Diego, La Jolla, California 92093, United States;* orcid.org/0000-0002-1809-5955

Ryan Wing − *Department of NanoEngineering, University of California, San Diego, La Jolla, California 92093, United States*

Timothy Pham − *Department of NanoEngineering, University of California, San Diego, La Jolla, California 92093, United States*

Complete contact information is available at: https://pubs.acs.org/10.1021/acs.analchem.0c01048

Notes

The authors declare no competing financial interest.

ACKNOWLEDGMENTS

The authors acknowledge funding from the National Institutes of Health through S10 OD023555-01A1, DP2 HL137187-S1, and T32 EB 009380. This material is based upon work supported by the National Science Foundation through NSF Grant 1845683 and the Graduate Research Fellowship Program under Grant No. DGE-1650112. C.M. also acknowledges support from the ARCS (Achievement Reward for College Scientists) Foundation. Transmission electron micrographs were taken in the Cellular and Molecular Medicine electron microscopy core facility, which is supported in part by NIH S10 OD021821. Figures 1 and 5A and TOC Figure were created with BioRender. The authors thank Dr. Kuba Tatarkiewicz for insightful scientific and technical discussion.

REFERENCES

(1) McElfresh, C.; Harrington, T.; Vecchio, K. S. *Meas. Sci. Technol.* **2018**, *29*, No. 065002.
(2) Lemaster, J. E.; Jeevarathinam, A. S.; Kumar, A.; Chandrasekar, B.; Chen, F.; Jokerst, J. V. *ACS Appl. Bio Mater.* **2019**, *2*, 4667−4674.
(3) Singh, P.; Bodycomb, J.; Travers, B.; Tatarkiewicz, K.; Travers, S.; Matyas, G. R.; Beck, Z. *Int. J. Pharm.* **2019**, *566*, 680−686.
(4) Mehta, D.; Jackson, R.; Paul, G.; Shi, J.; Sabbagh, M. *Expert Opin. Invest. Drugs* **2017**, *26*, 735−739.
(5) Rosenblum, W. I. *Neurobiol. Aging* **2014**, *35*, 969−974.
(6) Toyn, J. *What Lessons Can Be Learned from Failed Alzheimer's Disease Trials?*; Taylor & Francis, 2015.
(7) Gursky, O.; Aleshkov, S. *Biochim. Biophys. Acta* **2000**, *1476*, 93−102.
(8) Pryor, N. E.; Moss, M. A.; Hestekin, C. N. *Int. J. Mol. Sci.* **2012**, *13*, 3038−3072.
(9) Bartolini, M.; Naldi, M.; Fiori, J.; Valle, F.; Biscarini, F.; Nicolau, D. V.; Andrisano, V. *Anal. Biochem.* **2011**, *414*, 215−225.
(10) Janssen, L.; Sobott, F.; De Deyn, P. P.; Van Dam, D. *MethodsX* **2015**, *2*, 112−123.
(11) Pujol-Pina, R.; Vilaprinyó-Pascual, S.; Mazzucato, R.; Arcella, A.; Vilaseca, M.; Orozco, M.; Carulla, N. *Sci. Rep.* **2015**, *5*, No. 14809.
(12) Xue, C.; Lin, T. Y.; Chang, D.; Guo, Z. *R. Soc. Open Sci.* **2017**, *4*, 160696.
(13) Iadanza, M. G.; Jackson, M. P.; Hewitt, E. W.; Ranson, N. A.; Radford, S. E. *Nat. Rev. Mol. Cell Biol.* **2018**, *19*, 755−773.
(14) Liberta, F.; Loerch, S.; Rennegarbe, M.; Schierhorn, A.; Westermark, P.; Westermark, G. T.; Hazenberg, B. P.; Grigorieff, N.; Fändrich, M.; Schmidt, M. *Nat. Commun.* **2019**, *10*, No. 1104.
(15) Radamaker, L.; Lin, Y.-H.; Annamalai, K.; Huhn, S.; Hegenbart, U.; Schönland, S. O.; Fritz, G.; Schmidt, M.; Fändrich, M. *Nat. Commun.* **2019**, *10*, No. 1103.
(16) Gallagher-Jones, M.; Glynn, C.; Boyer, D. R.; Martynowycz, M. W.; Hernandez, E.; Miao, J.; Zee, C.-T.; Novikova, I. V.; Goldschmidt, L.; McFarlane, H. T.; et al. *Nat. Struct. Mol. Biol.* **2018**, *25*, 131.
(17) Brar, S. K.; Verma, M. *TrAC, Trends Anal. Chem.* **2011**, *30*, 4−17.
(18) Mahl, D.; Diendorf, J.; Meyer-Zaika, W.; Epple, M. *Colloids Surf., A* **2011**, *377*, 386−392.
(19) Tomaszewska, E.; Soliwoda, K.; Kadziola, K.; Tkacz-Szczesna, B.; Celichowski, G.; Cichomski, M.; Szmaja, W.; Grobelny, J. *J. Nanomater.* **2013**, *2013*, No. 313081.
(20) Ban, T.; Morigaki, K.; Yagi, H.; Kawasaki, T.; Kobayashi, A.; Yuba, S.; Naiki, H.; Goto, Y. *J. Biol. Chem.* **2006**, *281*, 33677−33683.
(21) Ban, T.; Yamaguchi, K.; Goto, Y. *Acc. Chem. Res.* **2006**, *39*, 663−670.
(22) Filipe, V.; Hawe, A.; Jiskoot, W. *Pharm. Res.* **2010**, *27*, 796−810.
(23) Yang, D. T.; Lu, X.; Fan, Y.; Murphy, R. M. *AIChE J.* **2014**, *60*, 1236−1244.
(24) Hlaing, M.; Gebear-Eigzabher, B.; Roa, A.; Marcano, A.; Radu, D.; Lai, C.-Y. *Opt. Mater.* **2016**, *58*, 439−444.

(25) Satinover, S. J.; Dove, J. D.; Borden, M. A. *Ultrasound Med. Biol.* **2014**, *40*, 138−147.
(26) Stetefeld, J.; McKenna, S. A.; Patel, T. R. *Biophys. Rev.* **2016**, *8*, 409−427.
(27) Tian, X.; Nejadnik, M. R.; Baunsgaard, D.; Henriksen, A.; Rischel, C.; Jiskoot, W. *J. Pharm. Sci.* **2016**, *105*, 3366−3375.
(28) Krueger, A. B.; Carnell, P.; Carpenter, J. F. *J. Pharm. Sci.* **2016**, *105*, 1434−1443.
(29) Zagorski, M. G.; Yang, J.; Shao, H.; Ma, K.; Zeng, H.; Hong, A. *Methods Enzymol.* **1999**, *309*, 189−204.
(30) Finder, V. H.; Glockshuber, R. *Neurodegener. Dis.* **2007**, *4*, 13−27.
(31) Gross, J.; Sayle, S.; Karow, A. R.; Bakowsky, U.; Garidel, P. *Eur. J. Pharm. Biopharm.* **2016**, *104*, 30−41.
(32) Parthasarathy, R. *Nat. Methods* **2012**, *9*, 724−726.
(33) Walker, J. G. *Meas. Sci. Technol.* **2012**, *23*, No. 065605.
(34) Berglund, A. J. *Phys. Rev. E* **2010**, *82*, No. 011917.
(35) Michalet, X. *Phys. Rev. E* **2010**, *82*, No. 041914.
(36) Michalet, X.; Berglund, A. J. *Phys. Rev. E* **2012**, *85*, No. 061916.
(37) Hartman, J.; Kirby, B. *Phys. Rev. E* **2017**, *95*, No. 033305.
(38) Ryan, T. M.; Caine, J.; Mertens, H. D.; Kirby, N.; Nigro, J.; Breheney, K.; Waddington, L. J.; Streltsov, V. A.; Curtain, C.; Masters, C. L.; et al. *PeerJ* **2013**, *1*, No. e73.
(39) Rambaldi, D. C.; Zattoni, A.; Reschiglian, P.; Colombo, R.; De Lorenzi, E. *Anal. Bioanal. Chem.* **2009**, *394*, 2145−2149.
(40) Schmit, J. D.; Ghosh, K.; Dill, K. *Biophys. J.* **2011**, *100*, 450−458.
(41) Amin, S.; Barnett, G. V.; Pathak, J. A.; Roberts, C. J.; Sarangapani, P. S. *Curr. Opin. Colloid Interface Sci.* **2014**, *19*, 438−449.
(42) Liu, J.; Nguyen, M. D. H.; Andya, J. D.; Shire, S. J. *J. Pharm. Sci.* **2005**, *94*, 1928−1940.
(43) Nicoud, L.; Lattuada, M.; Yates, A.; Morbidelli, M. *Soft Matter* **2015**, *11*, 5513−5522.
(44) He, F.; Becker, G. W.; Litowski, J. R.; Narhi, L. O.; Brems, D. N.; Razinkov, V. I. *Anal. Biochem.* **2010**, *399*, 141−143.
(45) Moore, K. A.; Pate, K. M.; Soto-Ortega, D. D.; Lohse, S.; van der Munnik, N.; Lim, M.; Jackson, K. S.; Lyles, V. D.; Jones, L.; Glassgow, N.; Napumecheno, V. M.; Mobley, S.; Uline, M. J.; Mahtab, R.; Murphy, C. J.; Moss, M. A. *J. Biol. Eng.* **2017**, *11*, No. 5.
(46) Jameson, L. P.; Smith, N. W.; Dzyuba, S. V. *ACS Chem. Neurosci.* **2012**, *3*, 807−819.
(47) Bieschke, J.; Russ, J.; Friedrich, R. P.; Ehrnhoefer, D. E.; Wobst, H.; Neugebauer, K.; Wanker, E. E. *Proc. Natl. Acad. Sci. U.S.A.* **2010**, *107*, 7710−7715.
(48) Palhano, F. L.; Lee, J.; Grimster, N. P.; Kelly, J. W. *J. Am. Chem. Soc.* **2013**, *135*, 7503−7510.
(49) Churches, Q. I.; Caine, J.; Cavanagh, K.; Epa, V. C.; Waddington, L.; Tranberg, C. E.; Meyer, A. G.; Varghese, J. N.; Streltsov, V.; Duggan, P. J. *Bioorg. Med. Chem. Lett.* **2014**, *24*, 3108−3112.
(50) Hoover, B. M.; Murphy, R. M. *J. Pharm. Sci.* **2020**, *109*, 452−463.
(51) Vestad, B.; Llorente, A.; Neurauter, A.; Phuyal, S.; Kierulf, B.; Kierulf, P.; Skotland, T.; Sandvig, K.; Haug, K. B. F.; Øvstebø, R. *J. Extracell. Vesicles* **2017**, *6*, No. 1344087.
(52) Kim, A.; Bernt, W.; Cho, N.-J. *Anal. Chem.* **2019**, *91*, 9508−9515.

https://dx.doi.org/10.1021/acs.analchem.0c01048
Anal. Chem. 2020, 92, 11590−11599